View metadata, citation and similar papers at core.ac.uk

brought to you by CORE

provided by NASA Technical Reports Server

RIACS

Research Institute for Advanced Computer Science
NASA Ames Research Center

A High Order Finite Difference Scheme with Sharp Shock Resolution for the Euler Equations

Margot Gerritsen and Pelle Olsson

RIACS Technical Report 96.01 January 1996

A High Order Finite Difference Scheme with Sharp Shock Resolution for the Euler Equations

Margot Gerritsen and Pelle Olsson

The Research Institute of Advanced Computer Science is operated by Universities Space Research Association, 10227 Wincopin Circle, Suite 212, Columbia, MD 21044, (410) 730-2656

Work reported herein was sponsored by NASA under contract NAS 2-13721 between NASA and the Universities Space Research Association (USRA). and by NSF Grant ASC 9318166–002

A HIGH ORDER FINITE DIFFERENCE SCHEME WITH SHARP SHOCK RESOLUTION FOR THE EULER EQUATIONS

MARGOT GERRITSEN AND PELLE OLSSON

ABSTRACT. We derive a high–order finite difference scheme for the Euler equations that satisfies a semi–discrete energy estimate, and present an efficient strategy for the treatment of discontinuities that leads to sharp shock resolution. The formulation of the semi–discrete energy estimate is based on a symmetrization of the Euler equations that preserves the homogeneity of the flux vector, a canonical splitting of the flux derivative vector, and the use of difference operators that satisfy a discrete analogue to the integration by parts procedure used in the continuous energy estimate. Around discontinuities or sharp gradients, refined grids are created on which the discrete equations are solved after adding a newly constructed artificial viscosity. The positioning of the sub-grids and computation of the viscosity are aided by a detection algorithm which is based on a multi–scale wavelet analysis of the pressure grid function. The wavelet theory provides easy to implement mathematical criteria to detect discontinuities, sharp gradients and spurious oscillations quickly and efficiently.

1. INTRODUCTION

High–order finite difference schemes are attractive for computing Euler flows that have large smooth flow regions. Their simplicity makes coding easy while their high order of accuracy allows for the use of coarse grids in the regions where the flow is slowly varying. In multi–dimensional applications this reduces both computational costs and memory requirements significantly. In the past, two problems prevented wide spread use of these schemes. Firstly, it was not known how to construct boundary difference operators of sufficient accuracy that lead to (strictly) stable numerical schemes. Secondly, the schemes introduce spurious oscillations at the shock that need to be damped by filtering or addition of artificial viscosity. Sharp shock resolution using previous techniques has required considerable tuning. In this paper we address both issues. We devise a high–order finite difference scheme that satisfies an semi–discrete energy estimate and present an efficient strategy for the treatment of discontinuities that leads to sharp shock resolution.

Stability of initial–boundary value problems can be ensured by the energy method. In general the method consists of an integration–by–parts procedure which introduces boundary terms that are subsequently bounded or eliminated to obtain the desired energy estimate. In [9, 17], Kreiss, Scherer and Olsson developed a semi–discrete analogue of this procedure for linear equations and special finite difference operators. Olsson showed that extension of the energy method to nonlinear systems is possible [18]. He employs a splitting of the flux derivative vector after symmetrization of the system. To facilitate the derivation of the energy estimates for the Euler equations, the variable transformation should preserve the homogeneity of the flux vector. We show that these conditions can be met for a specific class of transformations.

1991 *Mathematics Subject Classification.* 65M06,65M12.

This work has been sponsored by NSF Grant ASC 9318166–002 and by NASA under contract NAS 2–13721

Inspired by the stability results we devise a high–order scheme using the aforementioned transformation and splitting of the flux derivative vector. It results in a system of ordinary differential equations that is solved using a TVD Runge Kutta time integration. We refer to it as the Split High–Order Entropy–Conserving (SHOEC) scheme.

In the second and main part of the paper we present an efficient strategy for the treatment of discontinuities. Our purpose is twofold:

- Control spurious oscillations without sacrificing the overall computational efficiency of high–order methods.
- Resolve shocks sharply without having to adjust parameters.

In achieving these goals the stability properties of the method should not be destroyed. Our strategy is based on *local grid adaptation.* The smooth parts of the flow are resolved on coarse grids. Directly around the shocks finer sub-grids are constructed on which we solve the discrete equations after adding an artificial viscosity term. We use the grid adaptation techniques developed by Berger [1] and Zhu [25].

For schemes of even order, Gustafsson and Olsson [5] derived scalar artificial viscosities for conservation laws that support one– or two–point stationary and moving shocks. This theory does not directly apply to the Euler equations, but following a similar approach we can construct a scalar viscosity that supports near one–point shocks. The viscosity is determined completely by the flow variables on either side of the shock, and gives equally good results for the SHOEC–scheme.

The positioning of the sub-grids is aided by a detection algorithm based on a multi–scale wavelet analysis of the pressure grid function which locates potential shocks and spurious oscillations. It also supplies the information needed to compute the artificial viscosity terms. The detection algorithm is derived from a noise-detection algorithm developed by Mallat and coworkers [13, 14] in signal analysis.

Most existing shock detection algorithms search for maxima in the first or zero–crossings of the second derivative of grid functions. The derivatives are evaluated numerically at the scale of the grid. At this scale it is hard to distinguish between maxima that belong to spurious oscillations and those that correspond to shocks. Besides, it is difficult to extract information about the shock states when the discrete data are distorted by oscillations. If instead the grid function is analyzed on both the scale of the grid and a sequence of larger scales, these problems are resolved; the behavior at the larger scales is determined by phenomena such as shocks or sharp gradients, while local oscillations only influence the smaller scales. The number of available scales is limited because we work in a discrete and finite domain. The question is how to construct a reliable algorithm to determine the local behavior of the grid function based on this limited information. The *wavelet* theory supplies the answers. In a multi–scale wavelet analysis a function is convoluted with a family of wavelets, each varying in position and representing a different scale or frequency. For a special class of families a direct correlation exists between the local regularity of the function and the behavior of small, easy–to–determine, sets of wavelet coefficients. Moreover, they allow the formulation of a fast wavelet transform which leads to an efficient detection algorithm. The underlying wavelet theory is presented and the choice of the wavelet family is motivated. We thereby focus on issues that are relevant in the context of computational fluid dynamics.

The sharp shock resolution and the computational efficiency of the above described SHOEC–scheme with local grid adaptation are illustrated by numerical experiments for the one–dimensional Euler equations. Both shock detection and artificial viscosity are generalizable to multi–dimensions. We emphasize that the resulting scheme is a *shock–capturing* scheme as we do not require any a–priori knowledge of the shock location.

The paper is organized as follows. We start by presenting the Euler equations and relevant constitutive relations in section 2. Section 3 gives the derivation of the SHOEC–scheme. In section 4 the matrix and scalar viscosity are constructed. We give relevant wavelet theory, devise the shock detection algorithm and discuss specific implementation issues related to the Euler equations in section 5.

In the final two sections we present results and conclusions.

2. The Euler equations and relevant relations

The Euler equations in conservation form express the conservation of mass (ρ), momentum (m) and energy (E). They are given by

$$u_t + f(u)_x = u_t + f_u u_x = 0, \tag{2.1}$$

with state vector u and flux vector f of the form

$$u = \begin{bmatrix} \rho \\ \rho v \\ E \end{bmatrix}, \qquad f = \begin{bmatrix} \rho v \\ \rho v^2 + p \\ v(E+p) \end{bmatrix}. \tag{2.2}$$

The variables v and p are the velocity and pressure of the gas. The latter is related to u through the equation of state for a polytropic gas

$$p = (\gamma - 1)\left(E - \frac{1}{2}\rho v^2\right), \tag{2.3}$$

where $\gamma = 1.4$ is the ratio of specific heats c_p/c_v. The conservation of mass equation, $\rho_t = -(\rho v)_x = -m_x$, is often referred to as the continuity equation. The flux vector $f(u)$ is a homogeneous function of order one, i.e., $f(\theta u) = \theta f(u)$. The non-symmetric Jacobian matrix f_u is equal to

$$f_u = \begin{bmatrix} 0 & 1 & 0 \\ -(3-\gamma)\,v^2/2 & (3-\gamma)\,v & \gamma - 1 \\ (\gamma-1)\,v^3 - \gamma v E/\rho & \gamma E/\rho - 3(\gamma-1)\,v^2/2 & \gamma v \end{bmatrix}. \tag{2.4}$$

Its eigenvalues are $\lambda_1 = (v - c)$, $\lambda_2 = v$, and $\lambda_3 = (v + c)$, where $c = \sqrt{\gamma p/\rho}$ is the speed of sound.

Viscosity and thermal conduction are neglected in the formulation of the Euler equations. Because of the nonlinear and hyperbolic character of (2.1) shock waves can be formed at which these effects are of great importance. Additional jump conditions (the so called Rankine–Hugoniot conditions) are needed that relate the states u_l and u_r on the left and right sides of the shock wave. The Rankine-Hugoniot equations for a shock moving with a velocity s are

$$f_l - f_r = s(u_l - u_r). \tag{2.5}$$

The shock states u_l and u_r satisfy the Lax entropy conditions

$$\lambda_k(u_l) > s > \lambda_k(u_r), \qquad \lambda_{k-1}(u_l) < s < \lambda_{k+1}(u_r), \qquad k = 1, 3.$$

In order to simplify the analysis of the equations when there are finite jumps in u and f, Roe introduced the linearization

$$f_l - f_r = A^{lr}(u_l - u_r), \tag{2.6}$$

where $A^{lr} = f_u(\tilde{u})$ is the Jacobian matrix in the Roe–variables $\tilde{u}$, computed such that (2.6) is exact [20]. It follows from (2.6) and (2.5) that $\lambda_k^{lr} = s$. The vector $\tilde{u}$ is determined by

$$\tilde{\rho} = \sqrt{\rho_l \rho_r},$$

and the weighted averages

$$\tilde{v} = \frac{\sqrt{\rho_r}\,v_r + \sqrt{\rho_l}\,v_l}{\sqrt{\rho_l} + \sqrt{\rho_r}}, \qquad \tilde{H} = \frac{\sqrt{\rho_r}\,H_r + \sqrt{\rho_l}\,H_l}{\sqrt{\rho_l} + \sqrt{\rho_r}},$$

where H is the enthalpy of the system defined by $H = (E + p)/\rho$.

The entropy S given by

$$S = c_v \log(p\rho^{-\gamma}) + \textit{constant}.$$

is used in section 3 to formulate entropy functions of (2.1). In the remainder of this paper we will use a simplified scaled expression for the entropy of the form

$$S = \log(p\rho^{-\gamma}). \tag{2.7}$$

Smooth flows are isentropic, which means that

$$\frac{DS}{Dt} = \frac{\partial S}{\partial t} + u\frac{\partial S}{\partial x} = 0, \tag{2.8}$$

where D/Dt denotes the material derivative. In other words, the entropy is constant along streamlines for isentropic flows. Viscous effects and thermal conduction cause the entropy to increase over a shock and so equation (2.8) is valid outside shock regions only.

3. Deriving the SHOEC–scheme

We consider the system of conservation laws

$$\begin{aligned} u_t + f_x &= 0, \qquad u, f \in I\!R^d, \quad x \in (x_0, x_1), \quad t > 0, \\ u(x,0) &= \phi(x). \end{aligned} \tag{3.1}$$

At the boundaries $x = x_0$ and $x = x_1$ of the domain we prescribe data for the in-going characteristics in the general form

$$\omega_{\mathcal{I}}(x_i, t) = \psi_i(t), \quad i = 0, 1, \tag{3.2}$$

where $\omega_{\mathcal{I}}$ are the in-going characteristic variables.

We employ the energy method to ensure stability. The key to establishing an energy estimate lies in a special splitting of the flux derivative vector f_x, which we refer to as the *canonical splitting*, given by equation (3.6). To derive it we first write f_x as

$$f_x = (f - F)_x + F_x = (f - F)_x + F_u u_x, \tag{3.3}$$

where $F = F(u)$ satisfies Euler's inhomogeneous differential equation

$$\begin{aligned} F_u u &= -F + f, \\ F(0) &= f(0), \end{aligned} \tag{3.4}$$

and has the form

$$F(u) = \int_0^1 f(\theta u)\, d\theta. \tag{3.5}$$

Equations (3.3) and (3.4) now give the desired equation

$$f_x = (F_u u)_x + F_x = (F_u u)_x + F_u u_x. \tag{3.6}$$

The energy method applied to equation (3.1) yields

$$\frac{d}{dt}\|u\|^2 = -2(u, f_x) = -2(u, (F_u u)_x) - 2(u, F_u u_x).$$

The second equality follows from (3.6). If F_u is symmetric we obtain

$$\frac{d}{dt}\|u\|^2 = -2uF_u u\,|_{x_0}^{x_1}.$$

To arrive at a true energy estimate we need to control the boundary term $(uF_u u)$, for which we use the boundary conditions (3.2). However, these boundary conditions are related to f_u instead of F_u.

In order for the characteristic boundary condition to work we must require that f_u and F_u have the same inertia (i.e., the same number of positive and negative eigenvalues).

Equation (3.5) shows that F_u is symmetric provided f_u is symmetric. For the Euler equations this is not true however, and thus (2.1) must be symmetrized before the energy estimate can be derived.

3.1. Symmetrization using entropy functions. Symmetrization of systems (3.1) is possible through the use of entropy functions.

Definition 3.1. A scalar function η is an *entropy function* for a system of conservation laws (2.1) if

- η satisfies

$$\eta_u f_u = q_u, \tag{3.7}$$

  where $q(u)$ is a scalar function called the *entropy flux*, and $\eta_u = [\eta_{u_1}, \ldots, \eta_{u_d}]$ denotes the gradient of η.
- η is a convex function of u or, equivalently, $\eta_{uu} > 0$.

Multiplication of (2.1) by η_u shows that smooth solutions of this system also satisfy the scalar entropy equation

$$\eta_u u_t + \eta_u f_u u_x = \eta_t + q_x = 0. \tag{3.8}$$

Mock [16] proved that if an entropy function η exists for a system of equations (2.1) then the so called *entropy variables* w, given by $w^T = \eta_u$, symmetrize the system. This means that $u = u(w)$ and $\tilde{f}(w) = f(u(w))$ have symmetric Jacobians with respect to w. The transformed system is

$$u_t + f(u)_x = u_t + \tilde{f}(w(u))_x = u_w w_t + \tilde{f}_w w_x = 0. \tag{3.9}$$

Harten [6] derived a family of entropy functions using the equation for conservation of entropy (2.8). From this equation it follows that

$$\rho\, h(S)_t + \rho v\, h(S)_x = 0, \tag{3.10}$$

for all differentiable functions $h(S)$. If we multiply the continuity equation by $h(S)$ and add equation (3.10) we obtain

$$[\rho\, h(S)]_t + [\rho v\, h(S)]_x = 0.$$

This is precisely of the form (3.8) with $\eta \equiv \rho\, h(S)$ and $q \equiv \rho v\, h(S)$.

The entropy variables w determined by $w^T = \eta_u$ are

$$w = \frac{(\gamma-1)\dot{h}}{p} \left[E + \frac{p}{\gamma-1}(h/\dot{h} - (\gamma+1)) \quad -\rho v \quad \rho \right]^T. \tag{3.11}$$

The state vector u as a function of w reads

$$u = \frac{p}{(\gamma-1)\dot{h}} \left[w_3 \quad -w_2 \quad w_1 - \dot{h}(h/\dot{h} - (\gamma+1)) \right]^T. \tag{3.12}$$

The requirement that η be convex is equivalent to the requirement that w_u be positive definite because $w_u = \eta_{uu}$. Then, the transformation $w = w(u)$ is well-defined as w_u is nonsingular.

3.2. Energy estimates for the continuous and semi–discrete equations. To obtain the continuous energy estimate we apply the canonical splitting to the flux vector derivative $\tilde{f}_x$ and the u_t term. The latter splitting is possible because u_w is symmetric. Thus, we define the vector quantities $\tilde{U}(w)$, $\tilde{F}(w) \in I\!R^d$ that satisfy the equations

$$\begin{aligned} \tilde{U}_w w &= -\tilde{U} + u, \quad \text{and} \\ \tilde{F}_w w &= -\tilde{F} + \tilde{f}. \end{aligned}$$

As in (3.5) they satisfy

$$\tilde{U}(w) = \int_0^1 u(\theta w)\, d\theta, \qquad \text{and similarly} \tag{3.13}$$

$$\tilde{F}(w) = \int_0^1 \tilde{f}(\theta w)\, d\theta. \tag{3.14}$$

The above equations show that symmetry of u_w and $\tilde{f}_w$ implies symmetry of $\tilde{F}_w$ and $\tilde{U}_w$.

The canonical splitting of $\tilde{f}_x$ and u_t in (3.9) yields

$$(\tilde{U}_w w)_t + \tilde{U}_w w_t + (\tilde{F}_w w)_x + \tilde{F}_w w_x = 0.$$

We scalar multiply by w to get

$$(w^T \tilde{U}_w w)_t + (w^T \tilde{F}_w w)_x = 0, \tag{3.15}$$

and then integrate with respect to x which gives

$$\frac{d}{dt}\|w\|_{\tilde{U}}^2 = -w^T \tilde{F}_w w \,|_{x_0}^{x_1}, \quad \text{where} \tag{3.16}$$

$$\|w\|_{\tilde{U}}^2 = \int_{x_0}^{x_1} w^T \tilde{U}_w w \, dx. \tag{3.17}$$

Equation (3.13) shows that if u_w is positive definite $\tilde{U}_w$ is also positive definite, so the norm (3.17) is well defined.

Henceforth, we assume that $u(w)$ and $\tilde{f}(w)$ are both homogeneous functions in w:

$$\begin{aligned} u(\theta w) &= \theta^\beta u(w) \\ \tilde{f}(\theta w) &= \theta^\beta \tilde{f}(w) \end{aligned} \quad , \qquad \theta, \beta \in I\!R. \tag{3.18}$$

They satisfy Eulers differential equation, i.e., $\tilde{f}_w w = \beta w$ and $u_w w = \beta u$. The homogeneity of $\tilde{f}$ allows us to easily relate the right hand side of (3.16) to $\tilde{f}_w$ (inertia condition). The homogeneity of $u(w)$ is necessary in the derivation of the semi–discrete estimate. For the Euler equations we can construct entropy variables that satisfy these homogeneity constraints.

Equations (3.14) and (3.18) give

$$\tilde{F}(w) = \int_0^1 \theta^\beta d\theta \; \tilde{f}(w). \tag{3.19}$$

The integral exists if and only if $\beta > -1$ [1], in which case we have

$$\tilde{F}(w) = \frac{1}{\beta + 1} \tilde{f}(w), \quad \beta > -1. \tag{3.20}$$

---

[1]Note that a homogeneous function $\tilde{f}(w)$ satisfies Eulers differential equation $\tilde{f}_w w = \beta \tilde{f}$. If $\beta < 0$ and if $\tilde{f}$ is to be defined for all w in a neighborhood of 0, then $\tilde{f} \equiv 0$. However, in our applications at least one of the elements w_j of the vector w will be positive. Thus we can find a non zero solution of the form $\tilde{f}(w) = w_j^\beta g(\frac{w_1}{w_j}, \ldots, \frac{w_{j-1}}{w_j}, \frac{w_{j+1}}{w_j}, \ldots, \frac{w_d}{w_j})$ for some function g

Thus, we can write the canonical splitting of f_x as

$$f_x = \frac{1}{\beta+1}(\tilde{f}_w w)_x + \frac{1}{\beta+1}\tilde{f}_w w_x = \frac{\beta}{\beta+1}\tilde{f}_x + \frac{1}{\beta}\tilde{f}_w w_x. \tag{3.21}$$

Similarly we obtain

$$\tilde{U}(w) = \frac{1}{\beta+1}u(w), \quad \beta > -1, \tag{3.22}$$

and

$$u_t = \frac{\beta}{\beta+1}u_t + \frac{1}{\beta+1}u_w w_t. \tag{3.23}$$

Although integral (3.19) only exists for $\beta > -1$, the splittings (3.21) and (3.23) are valid for *all* $\beta \neq -1$ since $\tilde{f}_w w_x = \tilde{f}_x$ and $u_w w_t = u_t$ always hold.

Equation (3.20) leads to

$$\frac{d}{dt}\|w\|_{\tilde{U}}^2 = -\frac{1}{\beta+1} w^T \tilde{f}_w w \,|_{x_0}^{x_1}. \tag{3.24}$$

Furthermore

$$\|w\|_{\tilde{U}}^2 = \int_{x_0}^{x_1} w^T \tilde{U}_w w \, dx = \frac{1}{\beta+1}\int_{x_0}^{x_1} w^T u_w w \, dx \equiv \frac{1}{\beta+1}\|w\|_u^2.$$

The following estimate can now be shown [18]

$$\frac{d}{dt}\|w\|_u^2 \leq \psi_0^T \Lambda_{\mathcal{I}}(w(x_0,t))\psi_0 + \psi_1^T \Lambda_{\mathcal{I}}(w(x_1,t))\psi_1,$$

where $\Lambda_{\mathcal{I}}(w(x_i,t))$ are the absolute eigenvalues corresponding to the in-going characteristic variables at the boundary in question. As u_w and $\Lambda_{\mathcal{I}}$ both depend on w this is not an energy estimate in the usual sense. But as they are both positive definite we will refer to the inequality as a *generalized energy estimate.*

When discretizing the equations we apply the canonical splitting only to the spatial variables to retain a system of ordinary differential equations (ODEs). Using (3.21) the resulting semi-discrete equations are

$$\boldsymbol{u}_t = -\left(\frac{\beta}{1+\beta}\right) D\tilde{\boldsymbol{f}} - \left(\frac{1}{1+\beta}\right)\tilde{\boldsymbol{f}}_w D\boldsymbol{w}, \quad \beta \neq 1. \tag{3.25}$$

Here we use bold notation to distinguish discrete variables from continuous variables. Grid vectors like $\boldsymbol{u}$ are given by $\boldsymbol{u}^T = (\boldsymbol{u}_0^T, \boldsymbol{u}_1^T, \ldots, \boldsymbol{u}_n^T)$, where $\boldsymbol{u}_i \in I\!R^d, i = 0, \ldots, n$. The difference operator D is defined as

$$(D\boldsymbol{u})_j \equiv \frac{1}{h}\sum_{k=l}^{m_j} d_{jk}\boldsymbol{u}_k, \quad j = 0, 1, \ldots \tag{3.26}$$

The matrix $\tilde{\boldsymbol{f}}_w$ denotes the block diagonal matrix whose blocks are the Jacobians $\tilde{f}_w(w_i)$.

It can be shown [19] that $\boldsymbol{u}$ will satisfy the analytic boundary conditions if the initial and boundary data satisfy suitable compatibility conditions. In much the same way as in the continuous case, we can derive a generalized energy estimate for the semi-discrete equations (3.25) for difference operators that satisfy a summation-by-parts principle (B.1) [9, 23]. The second and fourth order difference operators that are used in the computations are given in appendix B. The second order operator is second order in the interior and first order on the boundary, and the fourth order operator is sixth order in the interior and third order on the boundary.

3.3. The entropy variables for the Euler equation. The homogeneity requirements of $\tilde{f}(w)$ and $u(w)$ restrict the choice of entropy function. Equation (3.12) shows that $u(w)$ is homogeneous provided the terms $h/\dot{h}$ and $(\gamma+1)$ in the expression for $u_1 = \rho$ have the same dimension. Thus, $h/\dot{h} \equiv \kappa$, where K is a constant, and consequently

$$h(S) = K\, e^{\kappa S} = K\,(p\rho^{-\gamma})^{\kappa}, \qquad K,\ \kappa \neq 0. \tag{3.27}$$

This exponential family leads to an homogeneous function $u(w)$ that satisfies $u(\theta w) = \theta^{\frac{1}{(1-\gamma)\kappa}} u(w)$ which follows from (3.12). Functions $h(S)$ of the form (3.27) were also discussed by Harten [6]. Following his notation we choose $\kappa \equiv 1/(\alpha+\gamma)$, $\alpha \in I\!R$. It follows that $\beta = (\alpha+\gamma)/(1-\gamma)$. Below it is shown that $\tilde{f}(w)$ has the same homogeneity constant. Thus, for $\alpha = 1-2\gamma$ the flux vector $\tilde{f}(w)$ is homogeneous of order one just as $f(u)$.

Now, (3.11) and (3.12) yield

$$w = \frac{p^*}{p}\left[\, u_3 + \frac{\alpha-1}{\gamma-1}p \quad -u_2 \quad u_1 \,\right]^T, \tag{3.28}$$

$$u = \frac{p}{p^*}\left[\, w_3 \quad -w_2 \quad w_1 - \frac{\alpha-1}{\gamma-1}p^* \,\right]^T, \tag{3.29}$$

where

$$p^* = \chi\, e^{S/(\alpha+\gamma)} = \chi\,(p\rho^{-\gamma})^{1/(\alpha+\gamma)}, \tag{3.30}$$

with $\chi = K^{\frac{\gamma-1}{\alpha+\gamma}}$. The variable p^* satisfies an equation similar to the equation of state (2.3)

$$p^* = \frac{(\gamma-1)}{\alpha}\left(\, w_1 - \frac{1}{2}\frac{w_2^2}{w_3} \,\right) \tag{3.31}$$

The pressure p can be expressed in terms of p^* and w as

$$p = \frac{1}{\chi}\left((p^*)^{\alpha}\, w_3^{\gamma}\right)^{1/(1-\gamma)}. \tag{3.32}$$

The flux vector

$$\tilde{f}(w) = \frac{p}{p^*}\left[\, -w_2 \quad \frac{w_2^2}{w_3} + p^* \quad -\frac{w_2}{w_3}\left(w_1 + \frac{\gamma-\alpha}{\gamma-1}p^*\right) \,\right]^T. \tag{3.33}$$

The homogeneity of $\tilde{f}(w)$ follows from equations (3.32),(3.31) and (3.33). The matrices w_u and $\tilde{f}_w$ are found in Appendix A. The convexity condition on the entropy function given by $\eta = \rho h(S)$ leads to the conditions $\chi < 0$, and $\alpha < -\gamma$ or $\alpha > 0$. This excludes the unacceptable case $\beta = -1$. We choose $\chi \equiv -1$.

The equations (3.25) are solved in time by the TVD Runge–Kutta scheme formulated in [22]. For the system of ODEs $\boldsymbol{u}_t = L(\boldsymbol{u}(\boldsymbol{w}))$, it computes the solution $\boldsymbol{u}^{n+1}$ at the $(n+1)st$ time step according to

$$\begin{array}{rcccccc} \tilde{\boldsymbol{u}}_1 &=& \boldsymbol{u}^n & & & + & \Delta t L(\boldsymbol{u}^n), \\ \tilde{\boldsymbol{u}}_2 &=& 3/4\,\boldsymbol{u}^n & + & 1/4\,\tilde{\boldsymbol{u}}_1 & + & 1/4\,\Delta t\, L(\tilde{\boldsymbol{u}}_1), \\ \boldsymbol{u}^{n+1} &=& 1/3\,\boldsymbol{u}^n & + & 2/3\,\tilde{\boldsymbol{u}}_2 & + & 2/3\,\Delta t\, L(\tilde{\boldsymbol{u}}_2), \end{array} \tag{3.34}$$

with time-step Δt and intermediate variables $\tilde{\boldsymbol{u}}_1$ and $\tilde{\boldsymbol{u}}_2$.
Here, $L(\boldsymbol{u}(\boldsymbol{w})) \equiv -\left(\frac{\beta}{1+\beta}\right) D\tilde{\boldsymbol{f}} - \left(\frac{1}{1+\beta}\right)\tilde{\boldsymbol{f}}_{\boldsymbol{w}} D\boldsymbol{w}$.

The variable p^* is the most computationally intensive term because of the exponentials in p and ρ. In the discrete equations (3.34) it appears in $\boldsymbol{w}_i$ and its reciprocal in $\tilde{\boldsymbol{f}}_i$. For isentropic flow the computations simplify; p^* is constant and is cancelled. We can use this simplification on the coarse

grid, outside the shock regions, where the flow is smooth. We note that for several values of α the computation of the exponential terms is fast. For $\alpha = 1 - 2\gamma$, for example, $p^* = -p^{-2.5}\rho^{-3.5}$.

3.4. Non–conservative form. It is well known that if a scheme is in conservative form, the computed shock speeds will be correct (see, e.g., [10]). This condition is sufficient, but not necessary. Tadmor [24] showed how to obtain second–order schemes for initial–boundary value problems that are entropy stable and in conservative form. It is however unknown if such schemes exist for higher orders of accuracy. The SHOEC scheme (3.25) is not written in conservative form. However, in experiments the shock speed has been found to be correct. Below, we show the error in shock location found for a single moving shock after long time integration (number of time steps is $\mathcal{O}(10^3)$) as a function of the step size. It is plotted against the step size. Computations are done in double precision. In all experiments, the error was of the order $h/10$. Clearly, we can draw the conclusion that the computed shock location is correct.

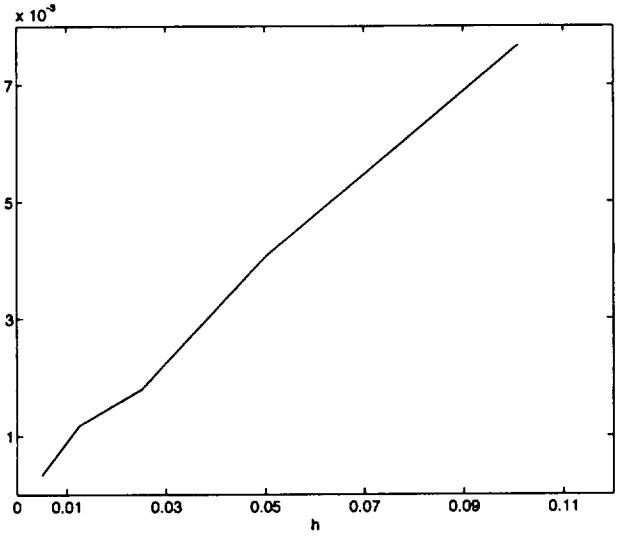

FIGURE 1. Error in shock location versus grid size h.

4. Scalar Artificial Viscosity

Artificial viscosity is added to the discrete scheme on the refined grids to control the spurious oscillations generated around shocks. We derive a scalar viscosity for conservative difference schemes of even order that gives approximate one–point stationary and moving shocks. It is determined by the flow variables and gives comparable results for the SHOEC scheme.

4.1. The shock profile. Following the approach in [5] we consider finite difference solutions of (2.1) with the Riemann initial condition

$$u(x,0) = \begin{cases} u_l & x < 0 \\ u_r & x \geq 0. \end{cases} \tag{4.1}$$

The shock states u_l and u_r are connected by a k–shock. For simplicity, we furthermore assume that u_l is the downstream (supersonic) shock state and that the flow is to the right, so that $\lambda_k = v - c$.

Applying the coordinate transformation

$$\begin{aligned} y &= x - st, \\ \tau &= t, \end{aligned}$$

(2.1) is changed to the stationary problem

$$(f - su)_y = 0, \qquad u(y,0) = \begin{cases} u_l & y < 0, \\ u_r & y \geq 0, \end{cases} \tag{4.2}$$

since $u_\tau = 0$ in the (y,τ)–coordinates. Adding artificial viscosity we discretize (4.2) as

$$D_0(\boldsymbol{f}_j - s\boldsymbol{u}_j) = h\, D_+ E D_- \boldsymbol{u}_j. \tag{4.3}$$

or, for constant E,

$$\boldsymbol{f}_{j+1} - \boldsymbol{f}_{j-1} - s(\boldsymbol{u}_{j+1} - \boldsymbol{u}_{j-1}) = 2E(\boldsymbol{u}_{j+1} - 2\boldsymbol{u}_j + \boldsymbol{u}_{j-1}). \tag{4.4}$$

E is a positive definite matrix. Scalar viscosities correspond to $E = \epsilon I, \epsilon > 0$, with I the identity matrix. The difference operators are defined by

$$D_0 \boldsymbol{u}_j = \frac{1}{2h}(\boldsymbol{u}_{j+1} - \boldsymbol{u}_{j-1}), \qquad D_+ \boldsymbol{u}_j = \frac{1}{h}(\boldsymbol{u}_{j+1} - \boldsymbol{u}_j), \qquad D_- \boldsymbol{u}_j = \frac{1}{h}(\boldsymbol{u}_j - \boldsymbol{u}_{j-1}),$$

where $h = x_{j+1} - x_j$ is the uniform mesh size.

The discrete system is subject to the boundary conditions

$$\lim_{j \to -\infty} \boldsymbol{u}_j = u_l, \qquad \lim_{j \to +\infty} \boldsymbol{u}_j = u_r.$$

4.2. Supporting approximate one–point shocks. We are interested in matrices E that support viscous shock profiles consisting of the states u_l, u_r and an intermediate state u_m. The state u_m is needed in practice to allow for the representation of shocks that are not positioned in the center of a grid cell [2].

We obtain the following equations at the points $x = -h$, $x = 0$, and $x = h$:

$$f_m - f_l - s(u_m - u_l) = 2E(u_m - u_l), \tag{4.5}$$

$$f_r - f_l - s(u_r - u_l) = 2E(u_r - 2u_m + u_l), \tag{4.6}$$

$$f_r - f_m - s(u_r - u_m) = 2E(u_m - u_r). \tag{4.7}$$

At all other grid points, the equations are trivially zero. The left hand side of (4.6) vanishes because of the RH conditions which gives $u_m = (u_r + u_l)/2$. As $f_r = f_l + s(u_l - u_r)$, equations (4.5) and (4.7) are in fact identical. For the Euler equations however, equation (4.5) can not be satisfied *exactly* for scalar viscosities $E = \epsilon I$ (see also [7]). Consider the equation corresponding to $f_1 = \rho v$ in (4.5):

$$\rho_l v_l - \rho_m v_m = (2\epsilon + s)(\rho_l - \rho_m). \tag{4.8}$$

We have $\rho_m = (\rho_l + \rho_r)/2$ and $\rho_m v_m = (\rho_l v_l + \rho_r v_r)/2$. Consequently,

$$\rho_l v_l - \rho_r v_r = (2\epsilon + s)(\rho_l - \rho_r). \tag{4.9}$$

The RH conditions require $\rho_l v_l - \rho_r v_r = s(\rho_l - \rho_r)$, and so $2\epsilon(\rho_l - \rho_r) = 0$, which cannot be fulfilled for $\epsilon > 0$. Also, for scalar E equations (4.5) and (4.7) lead to

$$f_m - f_l = (s + 2\epsilon)(u_m - u_l), \tag{4.10}$$

$$f_r - f_m = (s - 2\epsilon)(u_r - u_m). \tag{4.11}$$

Equation (4.10) represents a k–shock between states u_l and u_m moving with speed $(s + 2\epsilon)$, while (4.11) represents a k–shock between states u_m and u_r moving with speed $(s - 2\epsilon)$. The interaction between two such shocks generally results in the formation of a k–shock between u_l and u_r as well as

[2] (4.4) does not support zero–point shocks for $E > 0$. The left hand side of (4.4) vanishes because of the RH conditions. This leads to $E(u_l - u_r) = 0$, which can only be satisfied for $u_l = u_r$.

a contact discontinuity and a rarefaction wave [2] , whence the above described conflict for the Euler equations. But, assuming (4.10) and (4.11) are satisfied, a scalar viscosity can be derived that leads to approximate one–point shocks. Using Roe–linearization equation (4.10) becomes

$$A^{ml}(u_m - u_l) \;=\; (s + 2\epsilon)\,(u_m - u_l),$$

where A^{ml} is the Roe matrix determined by the states u_l and u_m. Thus, $(u_m - u_l)$ is an eigenvector of A^{ml} with eigenvalue $(s + 2\epsilon) = \lambda_k^{ml}$, or

$$\epsilon = 1/2(\lambda_k^{ml} - s)$$

to the left of the shock. Similarly, $\epsilon = 1/2(s - \lambda_k^{rm}) \approx 1/2(\lambda_k^{ml} - s)$ to the right of the shock. This choice of scalar artificial viscosity corresponds to that used by Jameson in [7]. Since $\lambda_k^l > s$, $\lambda_k^{lr} = s$ and the jump $[u_l - u_m]$ is less than the jump $[u_l - u_r]$, it can be expected that $\lambda_k^{lm} > s$ also. In practical applications we set $\epsilon = 1/2|(\lambda_k^{lm} - s)|$. We note that $|\lambda_k^{ml} - s| = \min_i |\lambda_i^{ml} - s|$. Similar analyses for other flow situations lead to the same choice

$$\epsilon = 1/2 \min_i \; |\lambda_i^{mp} - s|, \tag{4.12}$$

where u_p is the upstream state. For scalar equations, the equations (4.5), (4.6) and (4.7) are satisfied exactly for the above artificial viscosity. We note that also for systems (4.5) can be satisfied exactly if the matrix viscosity $E_m = (A^{lm} - sI)/2$ is used. However, E_m is not symmetric. So, even if its eigenvalues are all positive, E_m is not necessarily positive definite.

The scalar artificial viscosity is often chosen proportional to $\max_i |\lambda_i - s|$. Johansson and Kreiss [8] show that this viscosity indeed suppresses spurious oscillations, but leads to excessive smearing. They also recommend using $\min_i |\lambda_i - s|$, but evaluate the eigenvalue at u_l instead of u_{lm}, which in general leads to a larger viscosity.

We show the effectiveness of the artificial viscosity (4.12) for *stationary* shocks in figures 2a and 2b. They depict the pressure after long time integration of

$$\boldsymbol{u}_t \;=\; -D_0\boldsymbol{f} + hD_+ED_-\boldsymbol{u} \tag{4.13}$$

using the RK method (3.34) and the standard conservative scheme. The computations are done for $n = 100, D = D_0$, a CFL–number of 0.5 and varying Mach number without local grid adaptation. The numerical solutions are indicated by dotted lines and points in the shock region are highlighted. The solutions have negligible small amplitude oscillations.

SHOEC scheme We repeat the computations for the SHOEC scheme with artificial viscosity E

$$\boldsymbol{u}_t \;=\; -\left(\frac{\beta}{1+\beta}\right) D_0\tilde{\boldsymbol{f}} - \left(\frac{1}{1+\beta}\right) \tilde{\boldsymbol{f}}_w D_0\boldsymbol{w} + hD_+ED_-\boldsymbol{w}. \tag{4.14}$$

The results are shown in figures 3a and 3b, and are similar to those obtained with (4.13). This is expected as $\tilde{\boldsymbol{f}}_w D_0\boldsymbol{w} \approx D_0\tilde{\boldsymbol{f}}$ and so (4.14) and (4.13) should be close, at least for weak shocks. We remark that if a Roe–linearization $\tilde{f}_l - \tilde{f}_r = \tilde{A}^{lr}(u_l - u_r)$ can be found for the *symmetrized* Euler equations, the corresponding matrix viscosity $E_m \equiv |\tilde{A}^{lr} - sI|/2$ would be symmetric.

Assuming that the shock is located in the interior of the domain, E can be localized to a neighborhood of that shock; outside this region E would be identically zero. This is possible with a switch as defined in (4.21). Hence,

$$(w, D_+ED_-w)_h \;=\; -(D_-w, ED_-w)_h \;\leq\; 0. \tag{4.15}$$

Then, the addition of the term D_+ED_-w to an entropy conserving scheme will ensure an entropy inequality, i.e., the modified scheme is entropy stable. In particular, any scalar viscosity $E = \epsilon I$ will imply (4.15) and thus entropy stability.

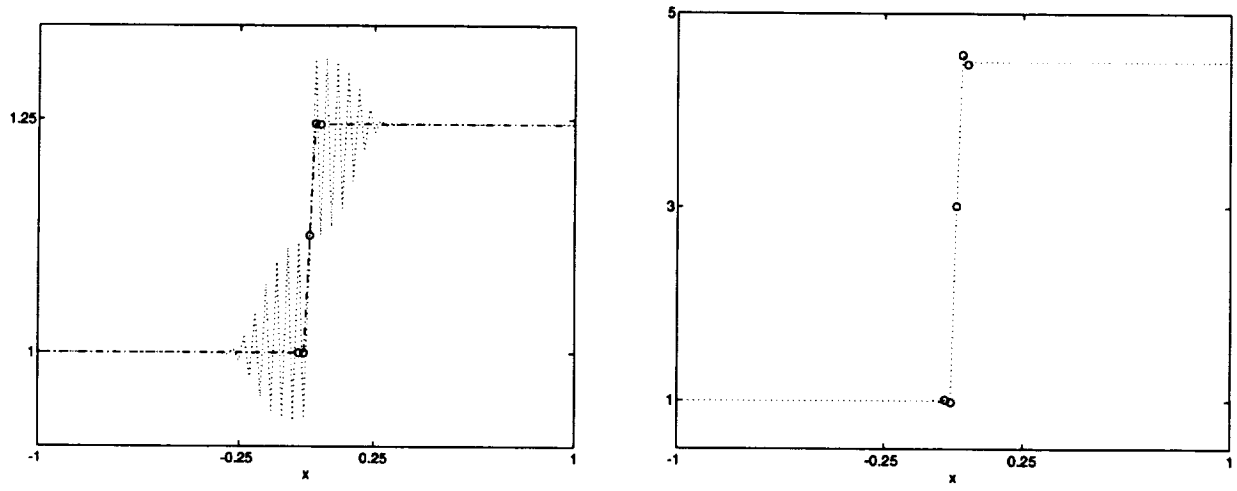

FIGURE 2. Standard central scheme, scalar viscosity, $t_{final} = 2, s = 0$; (a) $M = 1.1$, no viscosity (·), scalar viscosity (-.); (b) $M = 2, scalarviscosity$

Moving shocks Above, the equations are discretized on a grid that moves along with the shock, which is not the case in reality. Results for scalar equations are still satisfactory [5]. But, the damping by the viscosities is insufficient for the Euler equations as illustrated in figure 4a. This solution is computed with

$$E = 1/2|\, A^{lm} - sI \,| \equiv 1/2(Q|\, \Lambda^{ml} - sI \,|Q^{-1}), \tag{4.16}$$

where Λ^{ml} is the diagonal matrix containing λ_i^{ml}. For the scalar viscosity $\epsilon = 1/2 \min_i |\lambda_i^{ml} - s|$ an identical solution is obtained. We found experimentally that the strong oscillations are primarily generated in the k–th characteristic variable downstream of the shock. This is in agreement with the linear analysis by Johansson and Kreiss in [8]. They show that oscillations can appear in all characteristic variables upstream of the shock, but only in the k–th characteristic variable downstream of the shock, and that the amplitudes of the latter are generally much larger than those of the former. The matrix viscosity (4.16) does not introduce much damping on the k–th characteristic variable as $|\lambda_k^{ml} - s|$ is small. If we increase the damping by replacing this term with λ_2^{ml} in Λ^{ml} in (4.16) ($|\lambda_2^{ml} - s| > |\lambda_k^{ml} - s|$), the spurious oscillations indeed disappear. The result for this adapted matrix viscosity is shown in figure 4b.

We therefore choose the scalar viscosity equal to

$$\epsilon = \frac{1}{2} |\, \lambda_2^{ml} - s \,| \tag{4.17}$$

for moving shocks.

4.3. High order of accuracy. We consider the centered discretizations

$$\begin{aligned} Q_{2r} &= R_{2r}\, D_0, \qquad \text{with} \\ R_{2r} &= \sum_{\nu=0}^{r-1} (-1)^\nu \beta_\nu \, (h^2\, D_+\, D_-)^\nu, \end{aligned} \tag{4.18}$$

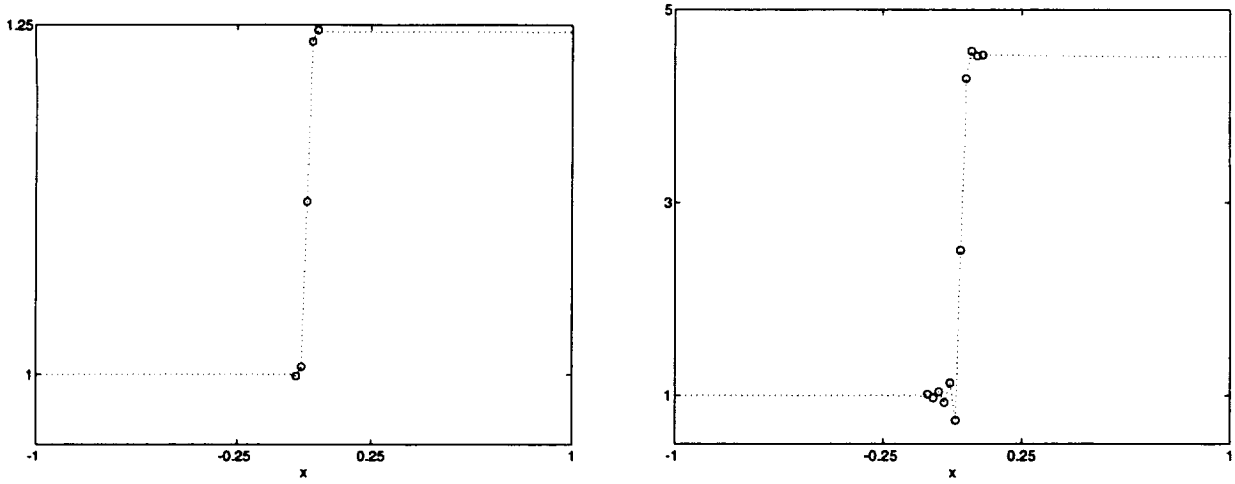

(a) (b)

FIGURE 3. SHOEC–scheme, scalar viscosity, $t_{final} = 2, s = 0$; (a) $M = 1.1$; (b) $M = 2$.

of order $2r$. The parameters β_ν are determined by

$$\begin{aligned} \beta_0 &= 1, \\ \beta_\nu &= \frac{\nu}{4\nu+2}\beta_{\nu-1}, \quad \nu = 1,2,\ldots,r-1. \end{aligned}$$

Appropriate approximations of the transformed equation (4.2) with artificial viscosity are

$$R_{2r}\, D_0 (f - s\boldsymbol{u})_j = h\, R_{2r}\, D_+\, E\, D_-\, \boldsymbol{u}_j, \tag{4.19}$$

where E and the boundary conditions are as before. In [5] it is shown that (4.19) holds if and only if (4.3) holds, and the results produced are the same. To take advantage of the high–order approximation property, we must implement the viscosity locally around the discontinuity. We use

$$R_{2r}\, D_0 (f - s\boldsymbol{u})_j = h\, R_{2r}\, D_+\, r_{j-1/2}\, E\, D_-\, \boldsymbol{u}_j, \tag{4.20}$$

where the switch r is defined by ([7])

$$r_j = \left(\frac{|\triangle_+ \boldsymbol{u}_j - \triangle_- \boldsymbol{u}_j|}{|\triangle_+ \boldsymbol{u}_j| + |\triangle_- \boldsymbol{u}_j| + \delta} \right), \qquad \delta << 1. \tag{4.21}$$

Hence, $r_j = 1$ at points where $\triangle_+ \boldsymbol{u}_j$ and $\triangle_- \boldsymbol{u}_j$ are of opposite sign, i.e., at points where the solution is oscillatory. In smooth flows $r_j << 1$. We define $r_{j-1/2} = (r_{j-1} + r_j)/2$. By positioning the switch and artificial viscosity as in (4.20) the viscosity terms are in conservative form.

5. DETECTION WITH WAVELETS

We want to detect shocks and spurious oscillations to aid the local grid adaptation procedure. The detection algorithm is based on a wavelet analysis of the pressure grid function. In the first part of this section we give a brief introduction to discrete wavelet families (5.1), motivate the choice of wavelet family and explain how the local behavior of a function can be determined from its wavelet transforms (5.2). The second part deals with implementation issues. The Fast Wavelet Transform (FWT) algorithm, introduced in 5.3, makes the detection algorithm computationally attractive. In 5.4 we discuss the implications of discrete grid functions, finite domains and the presence of spurious

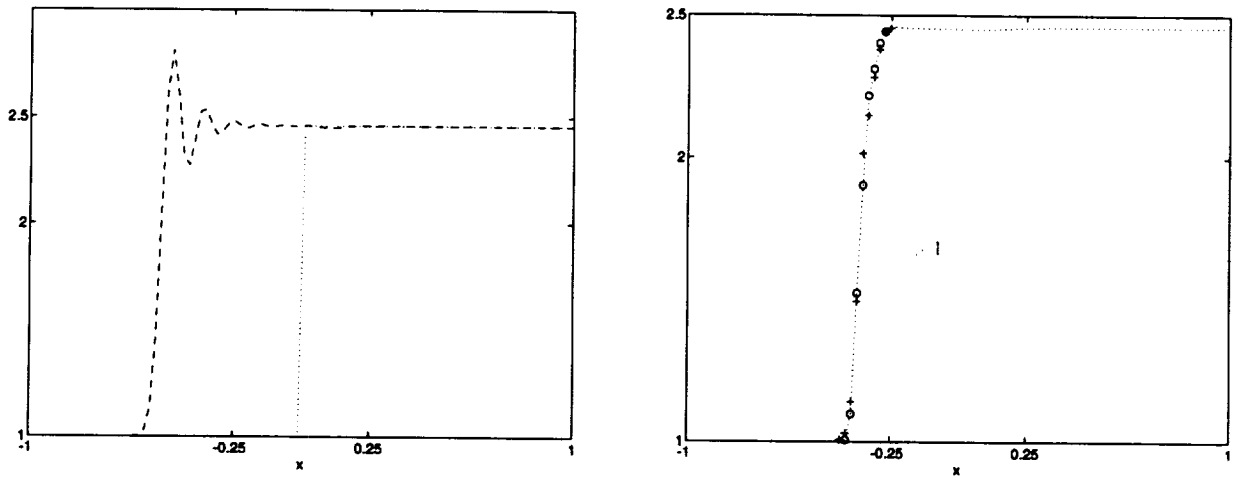

(a) (b)

FIGURE 4. Standard conservative scheme, moving shock, initially located at $x = 0$, $t_{final} = .3, M = 1.5$; (a) matrix viscosity (4.16), initial condition $(\cdot)$; (b) adapted matrix viscosity (o), adapted scalar viscosity (4.17) (+).

oscillations. At the end of the section we give a general outline of the detection algorithm. For a detailed description of the algorithm, including pseudo–code, we refer to [4]. We recommend Daubechies' book [3] for a thorough discussion of wavelet theory. The wavelet families used in the detection algorithm, and the underlying mathematical theory were developed by Mallat, Hwang and Zhong in [12, 13, 14].

5.1. Wavelets and discrete wavelet families. Roughly speaking a wavelet $\psi(x)$ is a well localized function that 'waves' above and below the x–axis such that $\int \psi(x)dx = 0$. [3] Dilations by $a \in I\!R^+$ and translations by $b \in I\!R$ of the mother wavelet $\psi(x)$ generate the wavelet family

$$\psi_{a,b}(x) \equiv \frac{1}{a}\psi\Big(\frac{x-b}{a}\Big). \tag{5.2}$$

The parameter b is the *center* of the wavelet $\psi_{a,b}$, and a represents its *scale*. A mother wavelet $\psi(x)$ and two members of the corresponding wavelet family are depicted in figure 5a. For $a > 1$ the wavelet $\psi_{a,b}$ stretches and can be viewed as representing a lower frequency, while for $a < 1$ the wavelet narrows and represents a higher frequency. Thus, the concepts of scale and frequency are closely related.

The continuous wavelet transform of a function $f \in L^2$ is given by

$$\langle f, \psi_{a,b} \rangle = \frac{1}{a}\int f(x)\,\psi\Big(\frac{x-b}{a}\Big)\,dx, \quad a \in I\!R^+, b \in I\!R \tag{5.3}$$

The variables $\langle f, \psi_{a,b}\rangle$ are referred to as the wavelet coefficients, and give information on the frequency content of f near the points b.

---

[3] Formally, a function $\psi(x)$ is said to be a wavelet if and only if its Fourier transform $\hat{\psi}(\omega)$ satisfies

$$\int_0^{+\infty} \frac{|\hat{\psi}(\omega)|^2}{\omega}\,d\omega = \int_{-\infty}^{0} \frac{|\hat{\psi}(\omega)|^2}{|\omega|}\,d\omega = C_\psi < +\infty. \tag{5.1}$$

This *admissibility condition* requires the wavelet to have sufficient decay in the frequency domain and that $\hat{\psi}(0) = 0$, which in turn leads to $\int \psi(x)dx = 0$.

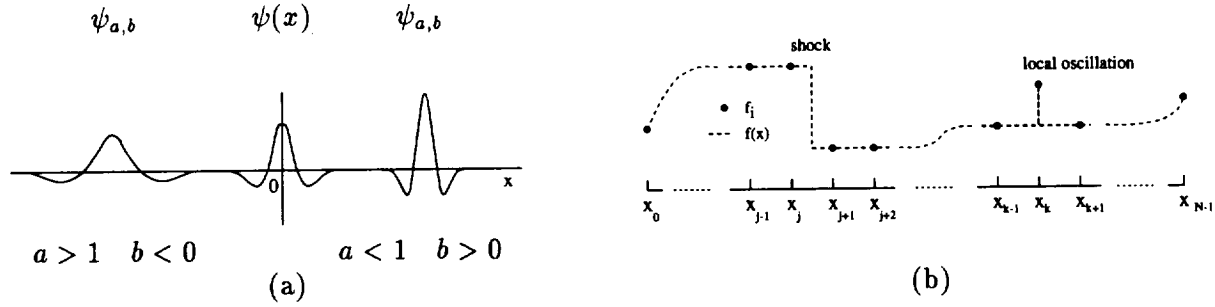

FIGURE 5. (a) Different members of the wavelet family; (b) Example of discrete function f_i and the corresponding continuous function $f(x)$.

For all practical purposes we are, of course, only interested in discrete values for a and b. The dilation parameter a is discretized as $a_m = 2^m, m \in \mathcal{Z}$, where m represents the level. The corresponding families are referred to as *dyadic* wavelet families and facilitate the formulation of Fast Wavelet Transform (FWT) algorithms (Sec. 5.3)

At each level m the wavelet coefficients are computed at the centers $b_{m,n} = n\triangle b, n \in \mathcal{Z}$, where $\triangle b$ may depend on m. This gives

$$\psi_{m,n} \equiv \psi_{2^m, b_{m,n}} = 2^{-m}\psi(\frac{x - n\triangle b}{2^m}), \quad m \in \mathcal{Z}. \tag{5.4}$$

To ensure that the wavelet coefficients contain enough information to characterize f, the family consisting of the wavelets $\psi_{m,n}$ must constitute a *frame* [3], i.e., there exist $0 < A \leq B < \infty$ such that, for all $f \in L^2$,

$$A\,\|f\|^2 \leq \sum_{m,n \in \mathcal{Z}} |\langle f, \psi_{m,n}\rangle|^2 \leq B\,\|f\|^2.$$

The case when $A = B = 1$ corresponds to $\{\psi_{m,n}\}$ being a basis. The choice of the mother wavelet $\psi(x)$ and the discretization of b are essentially only restricted by the frame and the admissibility conditions. The mother wavelet is normally chosen such that it is well concentrated in both the spatial and the frequency domain.

The detection algorithm is based on a wavelet analysis of the pressure grid function given by the discrete function f_i, with $i = 0, \ldots, N-1$. Consequently, m and n are bounded; the smallest scale that can be considered is determined by the grid size h, the largest scale is determined by the size of the domain, and the maximum number of points at which the wavelet coefficients can be evaluated is equal to N. Throughout this section, f_i is assumed to be the discrete representation of the function $f(x), x \in [x_0, x_{N-1}]$, To facilitate the discussion of the wavelet theory we consider functions $f(x)$ that can contain discontinuities at $x = x_{j+1/2}$, represented in the discrete domain by a jump between f_j and f_{j+1}, and local oscillations at $x = x_k$ when $(f_{k-1} - f_k) * (f_k - f_{k-1}) < 0$. Otherwise $f(x)$ is assumed to be slowly varying. An example is given in figure 5b. In section 5.4 we discuss grid functions that do not adhere to these simplifications, such as smeared shocks, grid functions with spurious oscillations around shocks, and grid functions that vary sharply in the vicinity of a shock.

5.2. Selection of the discrete wavelet family. The wavelet family is selected based on two criteria:

(1) There must exist a relation between the behavior of the wavelet coefficients and the local regularity of $f(x)$.
(2) The ensuing algorithm must be efficient, i.e., the number of wavelet coefficients needed to determine the local regularity of $f(x)$ with sufficient accuracy should be small.

For very special choices of $\psi(x)$ and with $\triangle b = 2^m$, the wavelet family $\psi_{m,n}$ constitutes an orthonormal basis. Many popular wavelet families, e.g. the Haar, Daubechies or Meyer wavelets, are members of this class. The orthogonal families satisfy the first criterion [3], but fail to meet the second in this application. To understand this, we observe that shocks and local oscillations may travel through the flow domain. The detection results should not change because of their movement, in other words, the wavelet transform should be *shift–invariant*. Figure 6a shows the centers in part of the scale–space (a, x) at which wavelet coefficients $\langle f, \psi_{m,n} \rangle$ are computed in an orthogonal wavelet analysis. We assume that f has a bounded discontinuity at $x_s = 0$, at which wavelet coefficients are computed at each scale. If the function is shifted by a distance of, for example, 2^j, only one wavelet coefficient is computed at the new location $x_s = 2^j$ at the levels shown. Also, the wavelet coefficients evaluated at positions close to x_s change as x_s is shifted. In practise, only a finite number of levels can be evaluated, and we expect that the detection results, which are based on this limited information, will change as well. Daubechies shows that indeed a very large number of levels is needed to accurately compute α for shifted singularities. Specifically, coefficients are needed at scales close to, or smaller than, the shift, which may not be available. So, orthogonal families are not suitable for detection purposes in the context of this paper; shift–dependency is unacceptable.

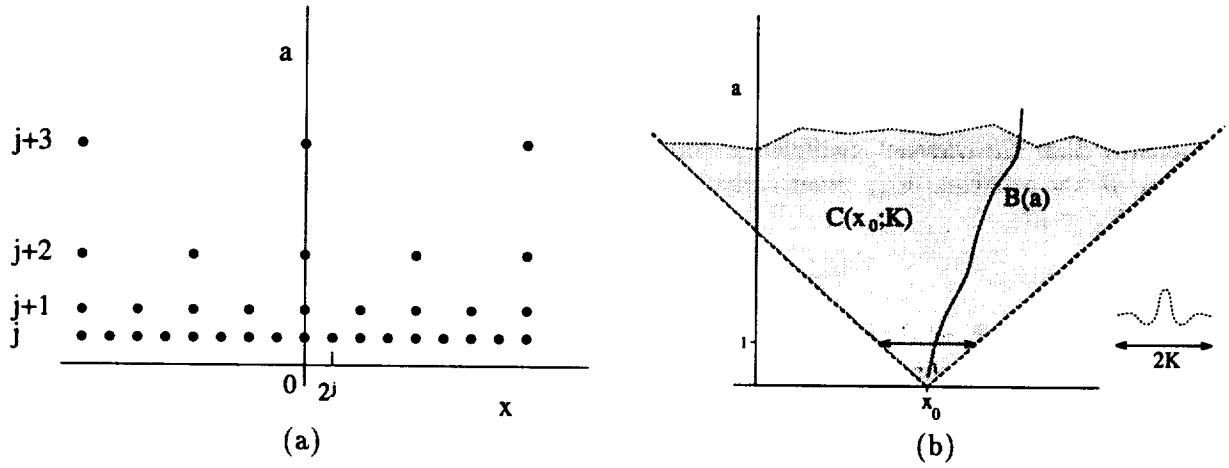

FIGURE 6. (a) Lattice of wavelet centers for orthogonal families; (b) Cone of influence of x_0.

Clearly, shift dependency can be avoided if the wavelet coefficients are computed at the same points at all scales, in other words, if $\triangle b = constant$. This constant, which represents the smallest scale possible, is determined by the grid size. Because the grid size h is not necessarily equal to a power or inverse power of 2, we normalize the smallest scale h to 1 (corresponding to $m = 0$). Then, $\triangle b \equiv 1$ in (5.4), which gives

$$\psi_{m,n} = 2^{-m} \psi(\frac{x - n}{2^m}), \quad m \geq 0. \tag{5.5}$$

This normalization is used in the remainder of the paper.

Having thus abandoned orthogonality, freedom in the design of the mother wavelet is gained. The question is if this freedom can be used to construct non–orthogonal families that satisfy the two criteria given above. Mallat and Hwang [13] showed that this is possible if the mother wavelet $\psi(x)$ has compact and symmetric support $[-K, K]$ for $K > 0$, and if it is a derivative of a smoothing function. Henceforth, all mother wavelets are assumed to be in this class. A smoothing function $\theta(x)$

is defined as a differentiable function that satisfies

$$\theta(x) > 0, \quad \int \theta(x)\,dx = 1, \quad \text{and} \quad \lim_{x \to \pm\infty} \frac{d^k \theta(x)}{dx^k} = 0, \quad k = 1, 2, \ldots . \tag{5.6}$$

From (5.6) it follows that $\int \psi(x)dx = 0$ for $\psi(x) \equiv d^k\theta/dx^k$ with $k > 0$. Provided $\psi(x)$ has sufficient decay in the frequency domain, it will satisfy the admissibility condition (5.1).

For such mother wavelets the local regularity of $f(x)$ can be computed from a small and easy–to–determine set of wavelet coefficients. The local regularity of a function is measured in terms of its Lipschitz exponent α, whose definition is given in appendix C. From this definition it follows that a continuous function has a Lipschitz exponent $\alpha > 0$, a bounded discontinuity (shock) is Lipschitz 0, and a Dirac function (local oscillation) has a Lipschitz exponent $\alpha = -1$. For ease of presentation, the theorem is presented for continuous wavelet families $\psi_{a,b} = \frac{1}{a}\psi(\frac{x-b}{a}), a \in I\!R^+, b \in I\!R$. First we make the following observation. If the support of the mother wavelet ψ is equal to $[-K, K]$, $\psi_{a,b}$ has support $[b - Ka, b + Ka]$. Thus, at any scale a, the function value $f(x_0)$ will influence the wavelet coefficients $\langle f, \psi_{a,b} \rangle$ computed at the centers b in the set

$$\mathcal{S}(a, x_0; K) \equiv \{\, b \,:\, |b - x_0| \leq Ka \,\}. \tag{5.7}$$

The region $\mathcal{C}(x_0; K) \equiv \cup_a \{a\} \times S(a, x_0; K)$ is referred to as the *cone of influence* of x_0 (figure 6b). It is intuitive to think that the local regularity of f at x_0 should be determined by the wavelet coefficients evaluated at centers in $\mathcal{C}(x_0; K)$. Mallat and Hwang [13] proved that this is true for the functions $f(x)$ considered in this paper. Mallat strengthened the result further in the following theorem:

Theorem 5.1. *Let θ be a smoothing function and let $\psi^k(x) = d^k\theta(x)/dx^k, k > 0$ have compact support $[-K, K]$. Let $b = B(a)$ be a curve in the cone of influence of x_0, with $B(a) \to x_0$ as $a \to 0$ (figure 6b). The function f is Lipschitz $\alpha < k$ at x_0, if there exists a constant $C > 0$ and a scale $\tilde{a}$ such that along any $B(a)$*

$$|\langle f, \psi_{a,b} \rangle| \leq C\, a^\alpha, \quad \forall a < \tilde{a}. \tag{5.8}$$

Define a modulus maximum at the scale a as a local maximum of $|\langle f, \psi_{a,b} \rangle|$ in b. The points b at which the modulus maxima are attained are referred to as the maximum points at scale a. If f has an isolated discontinuity at x_0, there exist a scale $\tilde{a}$ and a curve $b = B_M(a)$ such that for all $a < \tilde{a}$, $B_M(a)$ are maximum points. Such curves are referred to as maximum lines. The Lipschitz exponent of f at x_0 is determined by (5.8) evaluated along the maximum line converging to x_0.

A similar theorem also holds for dyadic families, with $a_m = 2^m$, and $b \in I\!R$ [15, 14]. However, we cannot compute coefficients at scales smaller than 1, nor at positions other than the grid points. Thus, we presume that the decay of the available wavelet coefficients at scales larger than 1 characterizes the regularity of the function. If this is not the case, the mesh must be refined (decreasing h). The second part of the theorem makes the wavelet detection computationally attractive; the Lipschitz exponent α at a point x_0 can be estimated from a limited number of wavelet coefficients. At a sequence of levels m, where $1 \leq m \leq m_{max} \leq \log_2(N)$, we compute the wavelet coefficients at the grid points. Next, we find the modulus maxima at each level and locate maximum lines that converge on the scale of the grid. Then, we determine α such that

$$\log_2 |\langle f, \psi^k_{m,n} \rangle| = \log_2 C + m\,\alpha, \tag{5.9}$$

as close as possible, in a least squares sense, for the wavelet coefficients along the select maximum lines.

As an example, figure 8b shows a signal with several points of distinct behavior, and the wavelet coefficients computed with the detection algorithm at increasing levels $j, j+1, \ldots$. If the Lipschitz exponent α is positive, the amplitude of the modulus maxima increases with j. The smooth variation

points 1 and 4 exhibit this behavior. The singularity at 3 produces modulus maxima that decrease as the scale increases, so $\sup(\alpha) < 0$. The amplitudes of the modulus maxima corresponding to point 2 do not change and we conclude that $\sup(\alpha) = 0$.

The parameter k limits the maximum Lipschitz exponent that can be determined. As we are interested in detecting discontinuities ($\alpha = 0$) and spurious oscillations ($\alpha < 0$), we choose $k = 1$. We remark that for $k = 1$, a direct connection exists between the wavelet detection and detection algorithms that search for maxima in derivatives. Define $\theta_{a,b} \equiv a^{-1}\theta(\frac{x-b}{a})$. The function $\theta_{a,b}$ is a smoothing function also as $\int \theta_{a,b}(x)dx = \int \theta(x)dx = 1$. Furthermore,

$$\psi_{a,b} = a\frac{d\theta_{a,b}}{dx},$$

so that

$$\langle f, \psi_{a,b} \rangle = \langle f, a\frac{d\theta_{a,b}}{dx} \rangle = -a\frac{d}{db}\langle f, \theta_{a,b} \rangle. \tag{5.10}$$

In other words, the wavelet transform is the first derivative of the function f smoothed at the scale a by $\theta_{a,b}$. So, detecting modulus maxima corresponds to detecting maxima in derivatives. It follows that a discontinuity has one maximum line converging to its location as the derivative of the smoothed function will have an absolute maximum at this position. A Dirac function naturally has two maximum lines. Furthermore, we note that the wavelet coefficients provide an estimate of the *jump* $[f]_a$ at scale a across the shock:

$$|[f]_a| = a\frac{|[f]_a|}{a} \approx a\left|\frac{d\langle f, \theta_{a,b}\rangle}{db}\right| = |\langle f, \psi_{a,b}\rangle|, \tag{5.11}$$

which can be used as an extra criterion for shock selection.

5.3. The Fast Wavelet Transform. For special $\psi(x)$ the wavelet transformations can be performed through fast discrete filter operations [4, 14]. Given two sequences $\{g_k\}_k$ and $\{h_k^m\}_k$, we define $G_m \equiv \{g_l^m\}_l$ and $H_m \equiv \{h_l^m\}_l$ as the sequences constructed by putting $(2^{m-1}-1)$ zeros between the elements of, respectively, $\{g_k\}_k$ and $\{h_k\}_k$. Also, $\mathcal{W}_m \equiv \{\langle f, \psi_{m,n}\rangle\}_n$ is defined as the sequence of wavelet coefficients at level m. It can be shown that certain $\psi(x)$ possess sequences $\{g_k\}_k$ and $\{h_k\}_k$ such that the wavelet coefficients at the levels $m \geq 1$ can be computed by the discrete convolutions

$$\begin{array}{rcl} \mathcal{W}_m & = & \frac{1}{\lambda_m} G_m * \mathcal{S}_{m-1} \\ \mathcal{S}_m & = & H_m * \mathcal{S}_{m-1} \end{array}, \quad m = 1, 2, \ldots \tag{5.12}$$

where the sequence $\mathcal{S}_0$ contains the grid function values f_i. The sequences $\mathcal{S}_m$ represent smoothed versions of f at level m, whereas $\mathcal{W}_m$ can be seen as representing the details lost in this smoothing process. For this reason, the sequence $\{h(k)\}_k$ is referred to as the impulse response of a *low pass* filter and $\{g(k)\}_k$ as the impulse response of a *high pass* filter. The finite resolution of $f(x)$ necessitates the scaling by the parameters λ_m. If the sequences $\mathcal{S}_m$ were available at all levels $m < 0$ (for $a_m \to 0$), the scaling parameters would not be needed. We refer to [4] for full details concerning their derivation. At each level m, we perform $\mathcal{O}(n)$ operations. The maximum number of levels is equal to $\log_2(n)$. For detection purposes it is sufficient to compute the wavelet coefficients at a total of four or five levels. Therefore, the overall detection algorithm is $\mathcal{O}(n)$. In the detection algorithm we use the mother wavelet depicted in figure 8b. It is a quadratic, anti-symmetric spline with compact support $[-1, 1]$ given by

$$\psi(x) = \begin{cases} 2(x+1)^2 & -1 \leq x < -1/2 \\ -4x(1+x) - 2x^2 & -1/2 \leq x < 0 \\ -4x(1-x) + 2x^2 & 0 \leq x < 1/2 \\ -2(x-1)^2 & 1/2 \leq x < 1 \end{cases} \tag{5.13}$$

Its filter coefficients h_k and g_k, and the scaling parameters λ_m are given in table 7. Note that symmetry is obtained by applying a shift of $1/2$ to $\mathcal{W}_m$.

Filter Coefficients			Scaling parameters			
k	h_k	g_k	m	λ_m	m	λ_m
-1	0.125		1	2	5	1.336
0	0.375	-2.0	2	1.5	6	1.334
1	0.375	2.0	3	1.375	7	1.333
2	0.125		4	1.344	> 7	1.333

FIGURE 7. Filter coefficients and scaling parameters for the spline wavelet

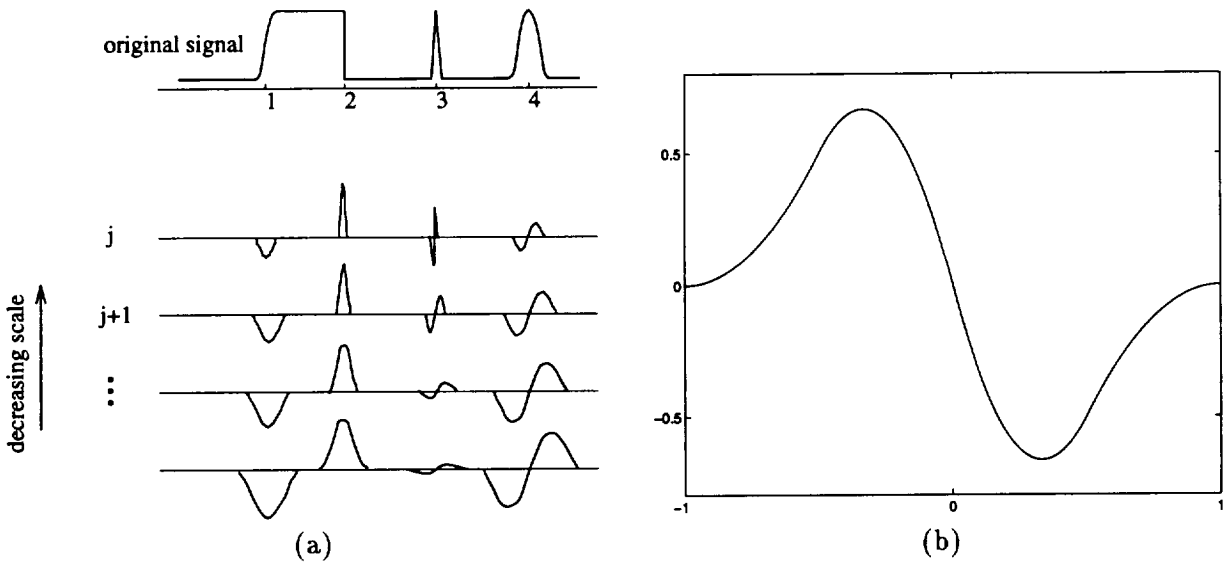

FIGURE 8. (a) Example wavelet transformation; (b) The spline wavelet ψ

5.4. Implementation issues. The pressure grid function f_i may be distorted by spurious oscillations around the shock. They are characterized by wavelength $L, L \geq 2h$ and amplitude r. Figure 9a shows the damping factors r_H/r and r_{HH}/r, where r_H and r_{HH} are the amplitudes of the smoothed oscillations after respectively one and two applications of H. Oscillations with a wavelength $L = 2h$ are removed immediately, and oscillations with short wavelengths are dampened quickly. Therefore, the oscillations have little and negligible effect on the computation of the Lipschitz coefficient α if we use levels $m \geq 2$ in (5.9). An example is given in figure 9b. It shows a pressure distribution obtained from a central finite difference scheme applied to the Euler equations. The oscillations are prominent at the smallest scale but quickly disappear. Note that the jump $|[f]|$ across the shock is accurately represented by the wavelet coefficients.

If a shock is smeared, the estimated Lipschitz exponent will be larger than zero. However, as the scale increases, the modulus maxima will quickly converge to a constant, equal to the total jump over the smeared shock. For one– and two–point shocks, the correct Lipschitz exponent can generally be detected from the modulus maxima at the levels $m \geq 3$. Otherwise, local oscillations and/or large magnitudes of the wavelet coefficients at the larger scales will indicate that there is a steep gradient necessitating local grid refinement. We remark that as a result of local grid refinement and an efficient artificial viscosity, smearing is generally not an issue at the coarser scales.

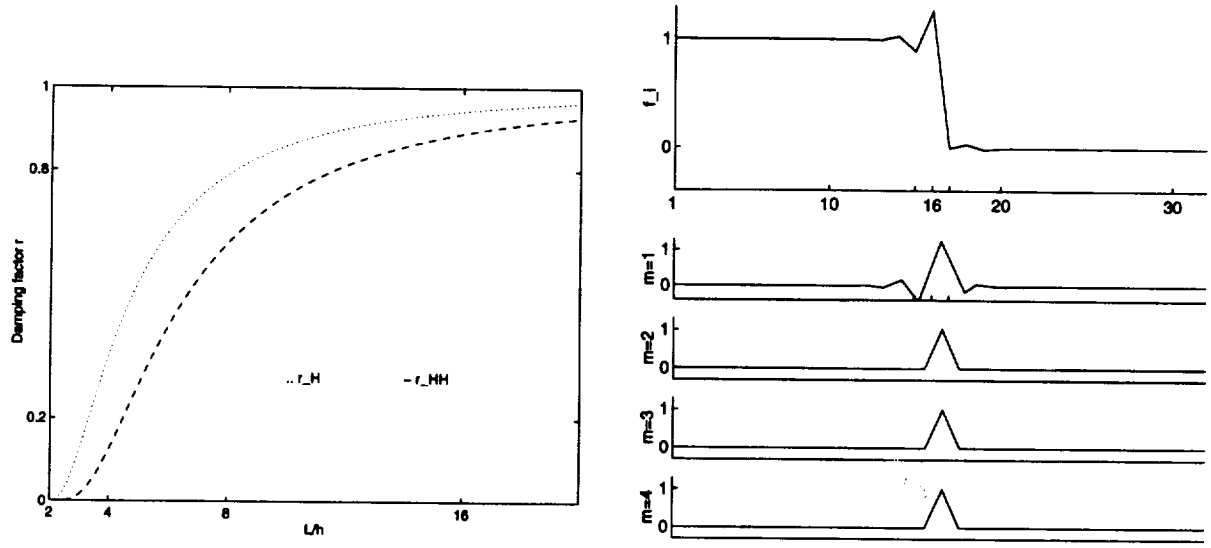

(a) (b)

FIGURE 9. (a) Damping Factors Filter H, and (b) Wavelet coefficients $\langle f, \psi_{m,n} \rangle$ corresponding to an oscillatory grid function f_i.

If the grid function varies sharply close to a discontinuity, the Lipschitz exponent will also be perturbed. However, the grid adaptation procedure will refine the grid locally as the detection algorithm will pick up local oscillations. At the finest scales, the variation in the grid function close to the shock will not be as strong and the discontinuity can again be detected with sufficient accuracy.

As the discrete domain is finite, we need to periodize f_i. To avoid the introduction of artificial shocks at the boundary, the finite discrete domain is extended by reflection according to

$$f_i = f_{2n-i}, \quad \text{for } n < i \leq 2n-1. \tag{5.14}$$

Although the reflected image is continuous at the boundary, its derivative may not be so. At the boundary itself this will not cause any problems because the filter G is anti–symmetric. In the local grid adaptation procedure, we ensure that the shocks are located in the interior of the (refined) grids, and that the flow varies smoothly near the boundaries. Therefore, the cusp or kink resulting from a discontinuous boundary derivative will be very small and will have negligible effect on the wavelet coefficients in the domain interior.

Approximations to the shock states u_l and u_r are needed to construct the artificial viscosity. If no local spurious oscillations are present, this task is trivial once the shock location is known. Otherwise, the data at the scale of the grid is distorted and we approximate f_L and f_R from the smoothed data $\mathcal{S}_m$ at scales $m \geq 1$.

We summarize the findings concerning the choice of the wavelet family:

- The family is dyadic for computational purposes.
- The family is redundant to obtain shift–invariance.
- The mother wavelet is compact, differentiable and the first derivative of a smoothing function so that theorem 5.1 is valid.
- A Fast Wavelet Transform exists, leading to an $\mathcal{O}(n)$ detection algorithm.

Below, a general outline of the detection algorithm is given with references to the relevant equations,

theorems and sections.

A general outline of the detection algorithm

	Reference
• Periodize the grid function f_i by reflection.	Eq. (5.14)
• Compute $\langle f, \psi_{m,n} \rangle$ in the extended domain at the scales $a_m = 2^m$, $m = 1, \ldots, m_{max}$ with a Fast Wavelet Transform.	Eqs. (5.12), (5.12), Table 7
• Locate the maxima of $\lvert\langle f, \psi_{m,n}\rangle\rvert$ at each scale.	
• Determine the converging maximum lines.	Thm. (5.1)
• Compute the Lipschitz exponents from the evolution of the wavelet coefficients along the converging maximum lines.	Eq. (5.9)
• Locate shocks, sharp gradients and spurious oscillations.	Sec. 5.2, 5.4

6. Numerical results

High order of accuracy

The initial conditions

$$u(x,0) = \begin{pmatrix} 1 + 0.5\cos(8\pi x) \\ u_1(x,0) \\ \frac{1}{\gamma - 1} + \frac{1}{2} u_1(x,0) \end{pmatrix} \tag{6.1}$$

with periodic boundary conditions, correspond to the linear advection of a cosine density wave. The velocity and pressure are equal to 1 and remain constant in time. This test problem is chosen to illustrate the advantage of difference operators with a high order of accuracy. The flow is smooth and therefore solved without local grid adaptation or artificial viscosity. Figure 10 depicts the solutions at $t = 0.3$ obtained for the SHOEC scheme with the sixth and second order difference operators given in the appendix [4], and the first order Godunov scheme for 50 grid points.

To achieve the same accuracy as the sixth order scheme, a minimum of 250 grid points is needed for the second order scheme and at least 2000 grid points for the first order scheme.

Shock detection, artificial viscosity and high order of accuracy

[4]Note that because of the periodic boundary conditions the global accuracy is sixth and second order respectively as well

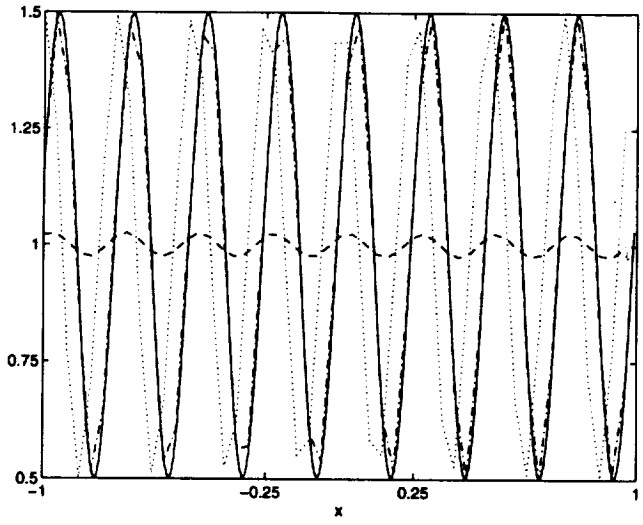

FIGURE 10. Solid line exact solution, 6th order (-.), 2nd order (·), 1st order (–).

We consider the initial condition

$$u(x,0) = \begin{cases} \begin{pmatrix} 3.857143 \\ 10.141852 \\ 39.166666 \end{pmatrix} & x < -4 \\ \begin{pmatrix} 1 + 0.2\sin 5x \\ 0 \\ 2.5 \end{pmatrix} & x \geq -4 \end{cases} \tag{6.2}$$

A strong shock wave, moving to the right, interacts with a sine wave of small amplitude. The shock speed $s = 3.55$, resulting in a Mach-number $M \approx 3$ in front of the shock. The difficulty lies in resolving the low and high frequency oscillations that are formed behind the shock wave in the density. This problem is a good test for resolution, as well as the detection algorithm and artificial viscosity. The solution is not known analytically. For comparison, an "exact" solution is computed using a formally conservative 4–th order central scheme with $n = 2000$ (no grid adaptation) and $t = 1$. The conservative form will ensure that the shock location is correct. The density is shown in figure 11a. Again, the computed solution is indicated by a dashed line and the points in the shock are highlighted. The shock is resolved very sharply which illustrates the effectiveness of the artificial viscosity.

Figures 11b and c show the coarse grid solutions for a fourth order SHOEC scheme (sixth order in interior and third order at the boundary) obtained for $n = 200$ and $n = 68$ respectively. We used local grid adaptation and one level of refinement (n is the number of coarse grid points). The shock location is determined with the detection algorithm; a priori knowledge of the shock speed is not used. The ratio of fine to coarse grid points is 4 for $n = 200$ and 8 for $n = 68$. We used the 4th order SHOEC scheme whose difference operator is given in appendix B (6th order in interior, 3rd order on the boundary). In figure 11d we depict the location of the fine grid relative to the coarse grid as time progresses for $n = 200$. The true and detected shock locations coincide. Clearly, the refined grid is confined to the shock region. The variations in fine grid size are due to spurious local oscillations away from the shock that are detected and included in the fine grid. The solution for $n = 200$ is very accurate. For $n = 68$ the fine grid solution is good and on the coarse grid the principal features of the flow are clearly visible. The average number of coarse and fine grid points in this last computation

is 150. The computation took approximately 8% of the time for $n = 2000$. The detection algorithm and the regridding procedure only accounted for 5% of the total time.

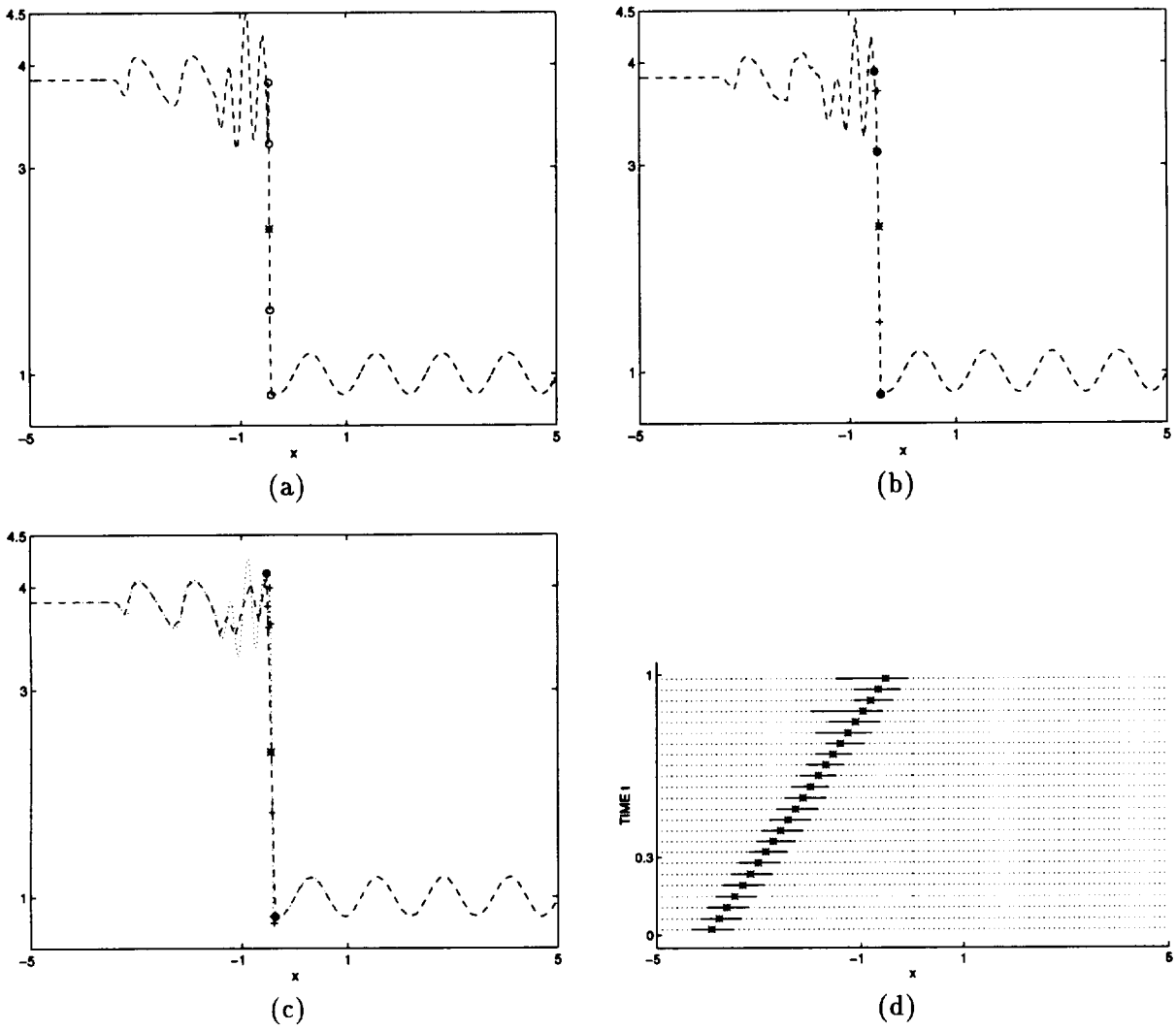

FIGURE 11. Density (a) conservative scheme, $n = 2000$; (b)+(c) local grid adaptation SHOEC scheme, coarse grid (–), fine grid (·), coarse grid point (o), fine grid point (+), true shock location (*); (b) $n = 200$; (c) $n = 68$; (d) Position of refined grid, $n = 200$, true and computed shock position (*).

7. CONCLUSIONS

We have presented a high order scheme for the Euler equations that satisfies a semi–discrete energy estimate, as well as an efficient strategy for computing sharp shock solutions. The high order of accuracy of this Split High–Order Entropy Conserving (SHOEC) scheme leads to a very efficient scheme for flows that are smooth in large regions of the flow domain. The construction of the SHOEC scheme is based on a symmetrization of the equations, followed by a canonical splitting of the flux vector, and difference operators that satisfy a summation by parts principle. The same techniques can be applied to other systems of conservation laws that satisfy the cone condition, mentioned in

section 3. We are currently developing a SHOEC scheme for mixed hyperbolic–parabolic equations in ocean modeling.

Although the scheme is in a non–conservative form, the shock location obtained in numerical experiments is correct and converges with h. This is illustrated in figure 1. In [21], Salas and Iollo formulated shock jump conditions for the Euler equations in their primitive, non–conservative, form. Jump conditions for the symmetrized split Euler equations are being investigated. Their existence may lead to an analytical explanation for the correct shock speed.

We constructed a cheap and effective scalar artificial viscosity that is used in locally refined grid in shock regions. It results in sharp shock resolution. The positioning of the finer sub-grids is aided by a detection algorithm based on a multi–scale wavelet analysis of the pressure grid function. The algorithm detects shocks and local oscillations efficiently. No a–priori knowledge of the shock location is used and the resulting method is therefore shock capturing. The obtained information on the shock position is used only in positioning the sub-grids and constructing the artificial viscosity. It could prove to be useful in other applications as well. As an example, we mention the high–order methods by LeVeque and Shuye [11] that need an accurate shock location.

The sharp shock resolution and computational efficiency of the above described SHOEC–scheme with local grid adaptation are illustrated by the numerical experiments.

The SHOEC scheme, artificial viscosity and shock detection are generalizable to multi–dimensions. In a forthcoming paper we will present numerical results for multidimensional applications in which we use the technique of overlapping grids as well as local grid adaptation.

Appendix A. Symmetrization

For $h(S) = e^{S/(\alpha+\gamma)}$,

$$\begin{aligned} w &= \frac{p^*}{p}\left[\, E + \frac{\alpha-1}{\gamma-1}p \quad -m \quad \rho \,\right]^T, \\ w_u &= \frac{p^*}{p^2} W, \end{aligned}$$

where

$$W = \begin{bmatrix} \frac{1}{\rho}\left(E\left(-\gamma R p + \tilde{R}\frac{m^2}{2\rho}\right) - \frac{\gamma}{\gamma-1}(\alpha-1)Rp\left(p+\frac{m^2}{2\rho}\right)\right) & -\frac{m}{\rho}\left(\tilde{R}E + (\alpha-1)Rp\right) & \tilde{R}E + (2-(\gamma+1)R)p \\ -\frac{m}{\rho}\left(\tilde{R}E + (\alpha-1)Rp\right) & -p + \tilde{R}\frac{m^2}{\rho} & \tilde{R}m \\ \tilde{R}E + (2-(\gamma+1)R)p & \tilde{R}m & \tilde{R}\rho \end{bmatrix}.$$

Here, p^* and p are related through equations (3.30) and (3.32),$R = 1/(\alpha+\gamma)$ and $\tilde{R} = (R-1)(\gamma-1)$. For $\alpha = (1-2\gamma)$, w is a homogeneous function of degree 1 in u, and

$$W = \gamma \begin{bmatrix} \frac{1}{\rho}\left(E\left(E - \frac{m^2}{\rho}\right) + \frac{2\gamma}{\gamma-1}p\left(p + \frac{m^2}{2\rho}\right)\right) & \frac{m}{\rho}\left(\frac{m^2}{\rho} - E\right) & \frac{1-3\gamma}{\gamma(1-\gamma)}p - E \\ \frac{m}{\rho}\left(\frac{m^2}{\rho} - E\right) & -\frac{p}{\gamma} - \frac{m^2}{\rho} & m \\ \frac{1-3\gamma}{\gamma(1-\gamma)}p - E & m & -\rho \end{bmatrix}.$$

The flux vector

$$\tilde{f}(w) = \frac{p}{p^*}\left[\, -w_2 \quad \frac{w_2^2}{w_3} + p^* \quad -\frac{w_2}{w_3}\left(w_1 + \frac{\gamma-\alpha}{\gamma-1}p^*\right) \,\right]^T.$$

The symmetric matrix $\tilde{f}(w)_w$ is given by

$$\tilde{f}_w = \frac{1}{p^*}\begin{bmatrix} Cm & C\rho v^2 - p & v(\frac{C}{2}\rho v^2 - \frac{\gamma}{\gamma-1}) \\ C\rho v^2 - p & v(C\rho v^2 - 3p) & \frac{C}{2}\rho v^4 - \frac{\gamma}{\gamma-1}\frac{p^2}{rho} - (\frac{3}{2} + \frac{\gamma}{\gamma-1})pv^2 \\ v(\frac{C}{2}\rho v^2 - \frac{\gamma}{\gamma-1}) & \frac{C}{2}\rho v^4 - \frac{\gamma}{\gamma-1}\frac{p^2}{\rho} - (\frac{3}{2} + \frac{\gamma}{\gamma-1})pv^2 & v(\frac{\gamma(1-2\gamma)}{(\gamma-1)^2}\frac{p^2}{\rho} + \frac{(1-2\gamma)}{\gamma-1}pv^2 + \frac{C}{4}\rho v^4) \end{bmatrix},$$

where $C = (1 - \alpha - \gamma)/\alpha$.

Appendix B. Difference Operators

We use difference operators that satisfy the summation by parts

$$(u, Dw)_h = u_n^T w_n - u_0^T w_0 - (Du, w)_h, \tag{B.1}$$

for arbitrary discrete grid vectors u and w, with respect to the weighted scalar product

$$(u, w)_h = h \sum_{i,j=0}^{n} \sigma_{ij} u_i^T w_j. \tag{B.2}$$

The scalar product can also be written as

$$(u, w)_h = h\, u^T \Sigma w. \tag{B.3}$$

To establish the semi-discrete estimate for the Euler equations, Σ must be diagonal [19]. In [9], Kreiss and Scherer showed that there exist diagonal Σ and difference operators D of accuracy $2p$ in the interior, $1 \le p \le 4$, such that the summation-by-parts property (B.1) holds. The difference operators D and matrices Σ are computed in [23].

The simplest example is the second order accurate difference operator

$$D = \frac{1}{h}\begin{bmatrix} -1 & 1 & & & \\ -0.5 & 0 & 0.5 & & \\ & \ddots & \ddots & \ddots & \\ & & -0.5 & 0 & 0.5 \\ & & & -1 & 1 \end{bmatrix},$$

with

$$\Sigma = \begin{bmatrix} 0.5 & & & & \\ & 1 & & & \\ & & \ddots & & \\ & & & 1 & \\ & & & & 0.5 \end{bmatrix}.$$

A sixth order accurate difference operator D with third order boundary closure is given by

$$(Du)_j = \begin{cases} \frac{1}{h}\sum_{i=0}^{i=8} d_{ji} u_i & j = 0, \ldots, 5 \\ \frac{1}{h}(-\frac{1}{60}u_{j-3} + \frac{3}{20}u_{j-2} - \frac{3}{4}u_{j-1} + \frac{3}{4}u_{j+1} - \frac{3}{20}u_{j+2} + \frac{1}{60}u_{j+3}) & 5 < j < n-5 \\ \frac{1}{h}\sum_{i=0}^{i=8} d_{ji} u_{n-i} & j = n-5, \ldots, n \end{cases}$$

The values of $d_{ji}, 0 \le j \le 5, 0 \le i \le 8$ are given below. The corresponding Σ is diagonal, i.e. $\sigma_{ij} = 0, i \neq j$. Its diagonal elements $\sigma_{ii} \equiv \sigma_i$ are

$$\begin{array}{lllll} \sigma_0 & = & \sigma_n & = & 13649/43200 \\ \sigma_1 & = & \sigma_{n-1} & = & 12013/8640 \\ \sigma_2 & = & \sigma_{n-2} & = & 2711/4320 \\ \sigma_3 & = & \sigma_{n-3} & = & 5359/4320 \\ \sigma_4 & = & \sigma_{n-4} & = & 7877/8640 \\ \sigma_5 & = & \sigma_{n-5} & = & 43801/43200 \end{array}$$

and

$$\sigma_j = 0 \qquad 5 < j < n-5$$

$$\begin{array}{llllll} d_{00} = -21600/13649 & d_{01} = 81763/40947 & d_{02} = 131/27298 \\ d_{03} = -9143/13649 & d_{04} = 20539/81894 & d_{05} = 0 \\ d_{06} = 0 & d_{07} = 0 & d_{08} = 0 \\ d_{10} = -81763/180195 & d_{11} = 0 & d_{12} = 7357/36039 \\ d_{13} = 30637/72078 & d_{14} = -2328/12013 & d_{15} = 6611/360390 \\ d_{16} = 0 & d_{17} = 0 & d_{18} = 0 \\ d_{20} = -131/54220 & d_{21} = -7357/16266 & d_{22} = 0 \\ d_{23} = 645/2711 & d_{24} = 11237/32532 & d_{25} = -3487/27110 \\ d_{26} = 0 & d_{27} = 0 & d_{28} = 0 \\ d_{30} = 9143/53590 & d_{31} = -30637/64308 & d_{32} = -645/5359 \\ d_{33} = 0 & d_{34} = 13733/32154 & d_{35} = -67/4660 \\ d_{36} = 72/5359 & d_{37} = 0 & d_{38} = 0 \\ d_{40} = -20539/236210 & d_{41} = 2328/7877 & d_{42} = -11237/47262 \\ d_{43} = -13733/23631 & d_{44} = 0 & d_{45} = 89387/118155 \\ d_{46} = -1296/7877 & d_{47} = 144/7877 & d_{48} = 0 \\ d_{50} = 0 & d_{51} = -6611/262806 & d_{52} = 3487/43801 \\ d_{53} = 1541/87602 & d_{54} = -89387/131403 & d_{55} = 0 \\ d_{56} = 32400/43801 & d_{57} = -6480/43801 & d_{58} = 720/43801 \end{array}$$

See [23] for a derivation of the coefficients.

Appendix C. Lipschitz exponent

Definition C.1 (Lipschitz exponent). Let $0 < \alpha < 1$.

(1) A function $f(x)$, defined on a domain $\mathcal{D}_f \subset I\!R$, is Lipschitz α over an interval $(x_l, x_r) \subset \mathcal{D}_f$, if and only if there exists a constant $C < \infty$ such that for all $x, y \in (x_l, x_r)$

$$|f(x) - f(y)| \le C\,|x - y|^{\alpha}.$$

(2) A function $f(x)$ is Lipschitz α at a point x_0, if and only if there exists a constant $C < \infty$ such that

$$\sup_{x \in \mathcal{D}_f} \frac{|f(x) - f(x_0)|}{|x - x_0|^{\alpha}} \le C.$$

(3) A function that is not Lipschitz 1 at a point x_0 is said to be singular at that point.

(4) A distribution is Lipschitz α over an interval (x_l, x_r), if and only if its primitive is Lipschitz $\alpha + 1$ on (x_l, x_r).

(5) A distribution $f(x)$ has an isolated singularity Lipschitz α at a point x_0, if and only if $f(x)$ is uniformly Lipschitz α over an interval (x_l, x_r) with $x_0 \in (x_l, x_r)$, and $f(x)$ is Lipschitz 1 over any subinterval of (x_l, x_r) that does not include x_0.

References

1. M. Berger and J. Oliger. Adaptive methods for hyperbolic partial differential equations. *Journal of Computational Physics*, 53:484–512, 1984.
2. R. Courant and K.O. Friedrichs. *Supersonic Flow and Shock Waves*. Springer–Verlag, 1948.
3. I. Daubechies. *Ten Lectures on Wavelets*. SIAM, 1992.
4. M. Gerritsen. Detecting shocks with wavelets: A tutorial. Technical report, SCCM, Stanford University, 1995.
5. B. Gustafsson and P. Olsson. High–order centered difference methods with sharp shock resolution. Technical Report RIACS–94.07, Research Institute of Advanced Computer Science, 1994.
6. A. Harten. On the symmetric form of systems for conservation laws with entropy. Technical Report ICASE 81-34, NASA Langley Research Center, 1981.
7. A. Jameson. Analysis and design of numerical schemes for gas dynamics 2, artificial diffusion and discrete shock structure. Technical Report RIACS 95-16, Research Institute of Advanced Computer Science, 1995.
8. G. Johansson and G. Kreiss. A note on the effect of artificial viscosity on solutions of conservation laws. Technical Report TRITA–NA–9219, Department of Numerical Analysis and Computational Science, Royal Institute of Technology Sweden, 1992.
9. H.-O. Kreiss and G. Scherer. On the existence of energy estimates for difference approximations for hyperbolic systems. Technical report, Department of Scientific Computing, Uppsala University, 1977.
10. R. LeVeque. *Numerical Methods for Conservation Laws*. Birkhaeuser Verlag, second edition, 1992.
11. R. J. LeVeque and K.-M. Shyue. One–dimensional front tracking based on high resolution wave propagation methods. *SIAM Journal of Scientific Computing*, 16(2):348–377, March 1995.
12. S. Mallat. Multiresolution approximation and wavelets. *Transactions of the American Mathematical Society*, 315:69–88.
13. S. Mallat and W.L. Hwang. Singularity detection and processing with wavelets. *IEEE Transactions Information Theory*, 38:617–643.
14. S. Mallat and S. Zhong. Characterization of signals from multiscale edges. *IEEE Transaction on Pattern Analysis and Machine Intelligence*, 14(7):47–67, 1992.
15. Y. Meyer. *Wavelets and Operators*. Cambridge University Press, 1992.
16. M. S. Mock. Systems of conservation laws of mixed type. *J. Differential Equations, 37 (1980), pp. 70–88.*
17. P. Olsson. Energy and maximum norm estimates for nonlinear conservation laws. Technical Report RIACS 94-01, Research Institute of Advanced Computer Science, 1994.
18. P. Olsson. Summation by parts, projections and stability. *Mathematics of Computation*, 64:1035–1065, 1995.
19. P. Olsson. Summation by parts, projections and stability III. Technical Report RIACS 95-06, Research Institute of Advanced Computer Science, 1995.
20. P.L. Roe. Approximate Riemann solvers, parameter vectors, and difference schemes. *Journal of Computational Physics*, 43:357–372, 1981.
21. M. D. Salas and A. Iollo. Entropy jump across an inviscid shock wave. Technical Report ICASE 95-12, NASA Langley Research Center, 1995.
22. C.-W. Shu. Total-variation-diminishing time discretizations. *Siam Journal on Scientific (and Statistical) Computing*, 9(6):1073–1084, Nov. 1988.
23. B. Strand. Summation by parts for finite difference approximations for d/dx. *Journal of Computational Physics*, 110(1):47–67, 1994.
24. E. Tadmor. Numerical viscosity and the entropy condition for conservative difference schemes. *Mathematics of Computation*, 43:353–368, 1984.
25. X. Zhu and J. Oliger. Stability and error estimation for component adaptive grid methods. Technical Report RIACS–94.14, Research Institute of Advanced Computer Science, 1994.

SCCM Program, Gates Building 2B, M/C 9025, Stanford University, Stanford CA 94305
E-mail address: margot@sccm.stanford.edu, olsson@sccm.stanford.edu

RIACS
Mail Stop T041-5
NASA Ames Research Center
Moffett Field, CA 94035